RSC Advances

PAPER

Check for updates

Graphene oxide supported titanium dioxide & ferroferric oxide hybrid, a magnetically separable photocatalyst with enhanced photocatalytic activity for tetracycline hydrochloride degradation

Wenxia Wang, [ID][a] Kaijun Xiao,*[a] Liang Zhu,[a] Yurong Yin*[b] and Zhaomei Wang[a]

A facile, robust approach to the synthesis of Fe_3O_4/rGO/TiO_2 nanocomposites is described. The synthesis involves two major steps: (1) preparation of Fe_3O_4/GO by an electrostatic self-assembly method; (2) deposition of TiO_2 on the surface of the Fe_3O_4/rGO nanocomposite *via* a hydrothermal method. The as-prepared Fe_3O_4/rGO/TiO_2 photocatalyst exhibited an enhanced photocatalytic activity for the degradation of tetracycline hydrochloride (TC-HCl) over a wide pH range from 3.0 to 11.0. At optimal conditions, a 92.6% degradation rate of TC-HCl was achieved within 330 min. The enhanced photocatalytic activity could be ascribed to the synergistic effect of the photo-Fenton reaction and electron transportation of graphene. A possible photocatalytic mechanism for TC-HCl by the Fe_3O_4/rGO/TiO_2 nanocomposite and H_2O_2 was proposed based on the quenching tests and liquid chromatography-mass spectrometry (LC-MS) analysis. Furthermore, a leaching test was also carried out and the result suggested that the leached iron from the reaction system was negligible and the catalyst still exhibited excellent photocatalytic activity after five reaction cycles, which clearly demonstrated that the Fe_3O_4/rGO/TiO_2 nanocomposite was reusable, excellently stable and highly effective.

1 Introduction

Recently, the widespread use and abuse of antibiotics, like tetracycline hydrochloride (TC-HCl), have aroused particular concern from scientists because of their extensive application to human beings, veterinary medicine, agriculture, aquaculture and planting.[1,2] As we all know that the excessive use of antibiotics may result in frequent detection of their residues in the environment because of their ineffective biological degradation,[3] which may lead to untreatable human disease. Besides, it is also a major concern that their persistent exposure to the environment may induce antibiotic-resistant genes. Currently, many methods, such as adsorption,[4] ion-exchange,[5] microbial degradation,[6] photocatalytic degradation,[7] electrolysis[8] and membrane filtration,[9] have been investigated for the removal of antibiotics. Among them, photocatalytic degradation was presented as an ideal method due to its high efficiency and low cost. However, the methodology is limited as most of the photocatalysts, such as TiO_2, SnO_2 and ZnO, can only respond to UV irradiation, which accounts for only 4–5% of solar light. Among the semiconductor catalysts, TiO_2 remains one of the most

promising photocatalyst candidates because of its easy availability, high oxidation efficiency, high photostability stability, nanotoxicity, chemical inertness, low cost and environmentally friendly nature.[10] However, the wide band gap (~3.2 eV) and intrinsic fast recombination of the photoexcited electron–holes of TiO_2 are big challenges to achieve higher photocatalytic efficiency and limits the TiO_2 application for large scale.[11] Recent years have witnessed a cornucopia toward the exploration of new TiO_2 photocatalyst. Up to now, numerous efforts, such as surface sensitization,[12] tuning the morphology,[13] noble metals or metal ions incorporation,[14] constructing heterojunctions[15] and transition metals and non-metals doping,[16] have been made to expand the photoresponse of TiO_2 catalyst into solar light and limit the recombination of photogenerated electron–hole pairs. As such, there is still an urgent need to explore a novel approach to remove antibiotics from aqueous solutions efficiently.

Impurities doping of TiO_2 (either cations or anions metals) and coupling TiO_2 with other semiconductors are the typical approaches to overcome the limitations of pure TiO_2.[17] Recently, photo-Fenton has received particular concern over the decades for the treatment of wastewater. From this point of view, TiO_2 nanoparticle can be introduced into the Fenton system to make a magnetically separable photo-Fenton catalyst with enhanced visible-light driven photocatalytic activity. However, the Fe_3O_4 nanoparticles are tend to aggregate and become large particles because of their strong anisotropic

[a]School of Food Science and Engineering, South China University of Technology, Guangzhou, 510640, China

[b]School of environment and energy, South China University of Technology, Guangzhou, 510640, China. E-mail: fekjxiao@scut.edu.cn; ppyryin@scut.edu.cn; Fax: +86-020-87113843; Tel: +86-020-87113843

dipolar interactions, which may affect their dispersibility and specific properties, thus diminishing their activity.[18] Hence, there is an urgent need to solve the existing problem. Taken together, it is worthwhile to introduce an effective interlayer between TiO_2 and Fe_3O_4 nanoparticles to maintain their special properties. Graphene has been demonstrated with unique atom-thick 2D structure, superior electron mobility, high specific surface area, excellent transparency, high chemical and electrochemical stability. As such, the graphene is attractive for photocatalyst carrier or promoter.[19]

Herein, we report a two-step process, an electrostatic self-assemble and hydrothermal method, to synthesis of $Fe_3O_4/$ rGO/TiO_2 photocatalyst. The catalytic properties of the as-prepared nanocomposite were further investigated in the discoloration and mineralization of TC-HCl in aqueous solution. The important operation variables, including initial solution pH, operation temperature, pollutant concentration and H_2O_2 concentration were systematically investigated to find the optimal operation conditions and provide guidance for the practical use of this catalyst. A possible photocatalytic mechanism for TC-HCl by $Fe_3O_4/rGO/TiO_2$ nanocomposites and H_2O_2 was proposed based on the quenching tests and liquid chromatography-mass spectrometry (LC-MS) analysis.

2 Experimental section

2.1 Materials

The majority of the chemicals, including ferric chloride hexa-hydrated ($FeCl_3 \cdot 6H_2O$), natural graphite flake, 3-aminopropyltrimethoxy-silane (APTMS) and tetrabutyl titanate (TBOT), were purchased from Aladdin Reagent Co., Ltd. (P. R. China), with their purity in analytical grade. The other chemical reagents were analytical grade and directly used as received. The tetracycline hydrochloride (TC-HCl) was bought from Aladdin Reagent Co., Ltd. (P. R. China). H_2SO_4 and NaOH solutions were used for pH adjustment. The structure of the TC-HCl is illustrated below:
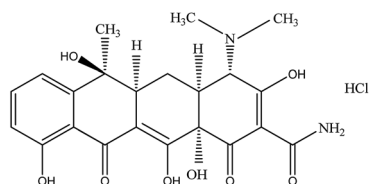
Chemical structure of the tetracycline hydrochloride (TC-HCl)

2.2 Synthesis of Fe_3O_4 nanoparticles

Fe_3O_4 nanoparticles were synthesized on the basis of a procedure reported previously.[20] In brief, 40 mL of ethylene glycol containing $FeCl_3 \cdot 6H_2O$ (1.35 g) was prepared under magnetic stirring. Then, predetermined amount of NaAc (3.6 g) and polyethylene glycol 4000 (1.0 g) were quickly added into the pre-mixed clear solution. The mixture was kept stirring for another 30 min and then transformed in to a 100 mL Teflon-lined stainless-steel autoclave, heated at 200 °C for 10 h. Finally, the

resultant solution was cooled down to room temperature naturally and then the precipitate was retrieved by centrifugation to give a black powder. The final product was washed three times with ethanol and distilled water and dried at 60 °C under vacuum.

2.3 Synthesis of Fe_3O_4/GO microsphere

GO was fabricated from natural graphite powder by following a modified Hummers protocol.[21] The Fe_3O_4/GO nanocomposites were prepared by a facile electrostatic self-assembly method. Briefly, 1 g of the Fe_3O_4 nanoparticles was sonicated for 1 h in 140 mL of isopropyl alcohol solution, and then the above mixture was kept stirring at 80 °C for 24 h with the addition of 1 mL APTMS. After complete reaction, the modified Fe_3O_4 microspheres were collected by centrifuged and washed three times by ethanol and distilled water, and then dried at 60 °C under vacuum. Thereafter, 0.1 g APTMS modified Fe_3O_4 nanoparticle was dissolved into isopropyl alcohol solution and then added dropwise into 150 mL of aqueous suspension of GO ($0.5~mg~mL^{-1}$) under mechanical stirring. The reaction was allowed to take place at room temperature for 24 h. Finally, the result nanocomposite was washed three times by ethanol and distilled water, and dried at 60 °C under vacuum.

2.4 Fabrication of $Fe_3O_4/rGO/TiO_2$ nanocomposite

$Fe_3O_4/rGO/TiO_2$ nanocomposite was synthesized by a facile hydrothermal method using Fe_3O_4/GO microsphere and tetrabutyl titanate (TBOT) as raw materials. In a typical synthesis, 30 mL of Fe_3O_4/GO microsphere was dissolved in 25 mL isopropyl alcohol and the resulting solution was obtained after ultrasonic for 30 min. Then 100 μL tetrabutyl titanate (TBOT) was added dropwise to the above solution under continuous mechanical stirring and kept stirring for 1 h. Afterward, 1 mL distilled water was added dropwise under mechanical stirring. The mixture was stirring for another 1 h before the mixture was transferred into a 100 mL Teflon-lined stainless steel autoclave for hydrothermal treatment at 180 °C for 8 h. After the autoclave cooled down to room temperature naturally, the final product was washed three times by absolute ethanol and distilled water, dried at 60 °C under vacuum.

2.5 Characterization method

The morphology and structure of $Fe_3O_4/rGO/TiO_2$ nanocomposite were characterized by transmission electron microscopy (TEM, Tecnai F20, 200 kV). The SEM images and EDS mapping was taken by the scanning electron microscopy (SEM, JSM 6701F). The zeta potential measurement was performed by using a Malvern zetasizer (Zetasizer 2000). The crystallographic and chemical bond analysis of the prepared materials were acquired by the X-ray diffractometry (Rigaku Miniflex XRD, Bruker) and Fourier transforms infrared spectroscopy (FTIR, VERTEX 33, Bruker). The X-ray photoelectron spectroscopy (XPS) (Kratos Axis Ultra DLD) of the catalyst was obtained from an axis-ultra X-ray photoelectron spectrometer with monochromatized Al-Kα radiation. The N_2 adsorption–desorption isotherms were recorded using the accelerated

surface area porosimetry system (ASAP 2020, Micromeritics). The vibrating sample magnetometry (VSM, LAKESHORE-7304) was used to assess the magnetic property at room temperature. Raman spectroscopy (LabRAM Aramis, Germany) was carried out on the samples at room temperature using a 785 nm Nd-YAG laser excitation source.

2.6 Photocatalytic degradation of tetracycline hydrochloride (TC-HCl)

Visible light-driven photocatalytic activity of each sample was measured in terms of the degradation of tetracycline hydrochloride (TC-HCl, 20 mg L^{-1}). In a typical experiment, a predetermined amount of Fe_3O_4/rGO/TiO_2 nanocomposite was suspended in 50 mL of TC-HCl solution (20 ∼ 120 mg L^{-1}). The suspension was kept stirring for 30 min in darkness to reach adsorption–desorption equilibrium. Then the suspension was irradiated with a 150 W Xenon lamp which was located with a distance of 10 cm at side of the reaction solution. At the predetermined time intervals, the analytical samples were withdrawn from the solution and immediately centrifuged at 8000 rpm for 1 min, then analysed using a spectrophotometer (UV-1801) at 356 nm.

In order to detect the active species during the photocatalytic reaction, benzoquinone (BQ), dimethylsulfoxide (DMSO), triethanolamine (TEOA), and isopropanol (IPA) were added into the TC-HCl suspension solution containing the 50% Fe_3O_4/rGO/TiO_2 composites photocatalyst to trap superoxide radicals ($^•O_2{}^-$), e$^-$, holes (h$^+$), and hydroxyl radicals ($^•OH$), respectively.

3 Results and discussion

3.1 Structural identification

The morphology of as-prepared Fe_3O_4, Fe_3O_4/GO and Fe_3O_4/rGO/TiO_2 was observed using SEM and TEM (Fig. 1). From Fig. 1a, we can see the spherical and uniform Fe_3O_4 microspheres and they all had very narrow diameter distributions, which can be more clearly seen at the TEM image illustrated in Fig. 1d. After assembly with GO nanosheets, the surface of the resulting binary nanoparticle became corrugated, which can be further conformed by the TEM image (Fig. 1e). This result indicated that there do exist thin layer on the surface of Fe_3O_4 particles due to the successfully integrating with GO. And the size of the binary nanoparticle of Fe_3O_4/GO became larger compared to that of the bare Fe_3O_4 particles. Shown in Fig. 1c, the as-prepared Fe_3O_4/rGO/TiO_2 nanocomposite reveal the like-sphere morphology in terms of size. The low-resolution TEM image in Fig. 1f further exhibit that the presence of uniform Fe_3O_4/rGO/TiO_2 nanocomposite resembling tiny rose petals around the like-sphere morphology, which may be attributed to the asymmetric deposition of the TiO_2 nanoparticles on the surface of the Fe_3O_4/GO microsphere induced by the slow kinetics associated with both reduction and surface diffusion.[22] The high-resolution TEM (HRTEM) image of the Fe_3O_4/rGO/TiO_2 nanocomposite is shown in Fig. 1g. There are two interplanar spacings (d = 0.230 and 0.290 nm) corresponding to (004) planes of anatase TiO_2 and (220) plane of Fe_3O_4,

respectively.[23] The related SAED pattern in Fig. 1h suggests the high crystallinity of TiO_2 nanoparticles. The positional distribution of Fe and Ti in the Fe_3O_4/rGO/TiO_2 nanocomposite was revealed by high-angle annular dark-field scanning TEM (HAADF-TEM) and EDX elemental mapping patterns. The HAADF-STEM image shows the different luminance in the signal Fe_3O_4/rGO/TiO_2 nanoparticle (Fig. 1i), manifesting that the Fe_3O_4/rGO/TiO_2 nanocomposites have a core–shell structure rather than an alloy structure.[24,25]

To gain insight into the crystal structure of the as-prepared samples, X-ray diffraction patterns of Fe_3O_4, anatase TiO_2, Fe_3O_4/TiO_2 and Fe_3O_4/rGO/TiO_2 were measured. Fig. 2a illustrated XRD pattern of the Fe_3O_4, the six characteristic peaks located at 18.25°, 29.98°, 36.37°, 43.47°, 53.77°, 57.28° and 63.14° are indexed to (111), (220), (311), (400), (422), (511) and (440), respectively. The results agree well with the typical structure of Fe_3O_4 nanoparticles [JCPDS: 19-0629].[26] Typical sharp and intense peaks observed in Fig. 2b can be attributed to the anatase phase of TiO_2 (JCPDS 21-1272). In fact, similar result is also reported in the former literature.[27] The XRD pattern of the Fe_3O_4/TiO_2 and Fe_3O_4/rGO/TiO_2 shown in Fig. 2a match both the Fe_3O_4 nanoparticles and the anatase TiO_2, which conformed that the TiO_2 nanoparticles were successfully installed on the surface of the Fe_3O_4 nanospheres and Fe_3O_4/GO composites.[28] The FTIR spectra of anatase TiO_2, Fe_3O_4, Fe_3O_4/TiO_2 and Fe_3O_4/rGO/TiO_2 are recorded in Fig. 2b. For anatase TiO_2 (Fig. 2b), the peak located at 583 cm^{-1} is attributed to stretching vibration of Ti–O–Ti bond, which is consistent with previous literature.[29] As can be seen from Fig. 2b, the strong absorption peak at 582 cm^{-1} correspond to the Fe–O stretching vibration of Fe_3O_4. Meanwhile, in comparison with Fe_3O_4/TiO_2, the peaks at 1258 cm^{-1} and 1073 cm^{-1} can be attributed to C–O in COH/COC of the GO, which indicates that the GO was not completely reduced.

The magnetic properties of the as-obtained materials were characterized by a vibrating sample magnetometer at room temperature. As illustrated in Fig. 3a, the saturation magnetization values of Fe_3O_4 NPs, Fe_3O_4/GO and Fe_3O_4/rGO/TiO_2 nanocomposite are 215.0, 50.84 and 20.0 emu g^{-1}, respectively. It is worth noting that the saturation magnetization value of the nanocomposites decreased sharply after coating with the TiO_2 or GO sheet, which are the non-magnetic nanocomposites content in the hybrids that reduce the magnetization.[26] However, the Fe_3O_4/rGO/TiO_2 still exhibited good magnetic properties that can ensure them be easily collected and recycled from aqueous solution by simply putting an external magnetic field. The inset of Fig. 3a shows the attraction of the Fe_3O_4/rGO/TiO_2 nanoparticles to a commercial magnet in 1 min. The nanoparticles homogeneously dispersed in liquid could be easily collected by an external magnetic field, which conformed their excellent superparamagnetic property. Fig. 3b shows the UV-vis absorbance of GO and Fe_3O_4/rGO/TiO_2. It is evident that the UV absorption peak of the GO and Fe_3O_4/rGO/TiO_2 appears at 227 nm and 257 nm, respectively. The red-shift may be caused by the formation of chemical bond between GO and Fe_3O_4.[30]

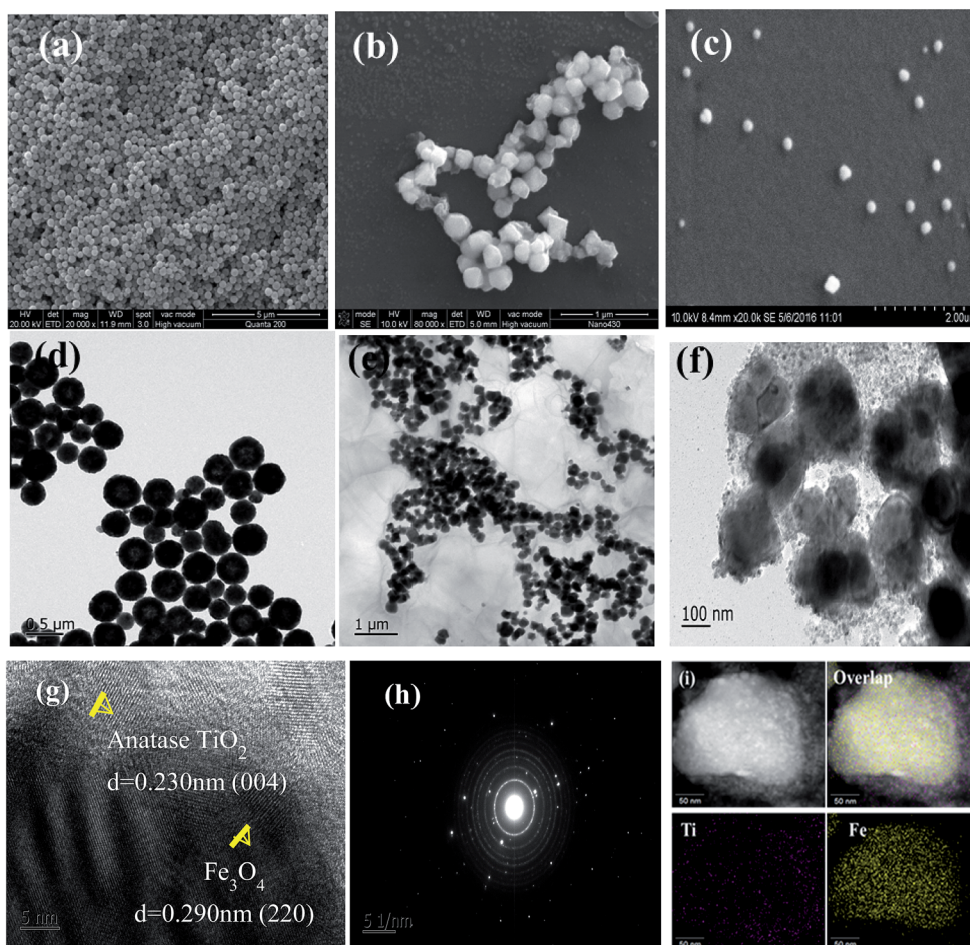Raman spectroscopy was used to fully understand the structure and crystalline phase of the Fe_3O_4/rGO/TiO_2

Fig. 1 Typical SEM image (a–c) and TEM (d–f) image of Fe_3O_4, Fe_3O_4/GO, Fe_3O_4/rGO/TiO_2 nanocomposite (g) HRTEM image of Fe_3O_4/rGO/TiO_2 nanoparticles, (h) selected area electron diffraction pattern (SAED) pattern of Fe_3O_4/rGO/TiO_2 nanocomposite (i) HAADF-STEM image of the individual Fe_3O_4/rGO/TiO_2 nanoparticle and the corresponding elemental mapping images of Fe_3O_4/rGO/TiO_2 nanocomposite.

nanocomposite. It is obvious from Fig. 4a that the Fe_3O_4/rGO/TiO_2 hybrids show the typical Raman peaks of Fe_3O_4/TiO_2 and Fe_3O_4/GO. Besides, the value of I_D/I_G for Fe_3O_4/rGO/TiO_2 hybrids ($I_D/I_G = 1.18$) is higher than for pure Fe_3O_4/GO ($I_D/I_G = 0.89$), which indicates the successful transformation of GO to r-

GO through hydrothermal.[31] Taking a detailed look at the Raman spectra of TiO_2 and Fe_3O_4/TiO_2 (Fig. 4b), it is clear that the Raman peaks appear at 142, 195, 395, 516, and 639 cm^{-1} are ascribed to vibration modes of $E_{g(1)}$, E_g, B_{1g}, $A_{1g} + B_{1g}$, and $E_{g(2)}$, respectively.[32,33] The result is consistent with the XRD analysis.
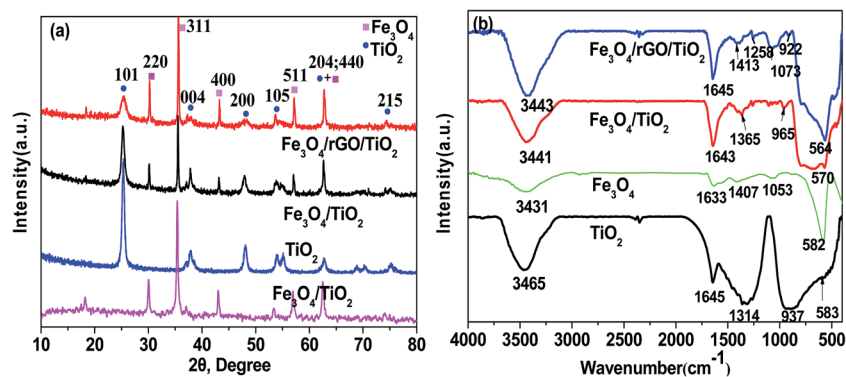
Fig. 2 XRD patterns (a) and FTIR spectra (b) of Fe_3O_4, anatase TiO_2, Fe_3O_4/TiO_2 and Fe_3O_4/rGO/TiO_2. The blue spheres (●) and pink cubes (■) indicate the typical diffraction peaks of anatase TiO_2 and Fe_3O_4, respectively.
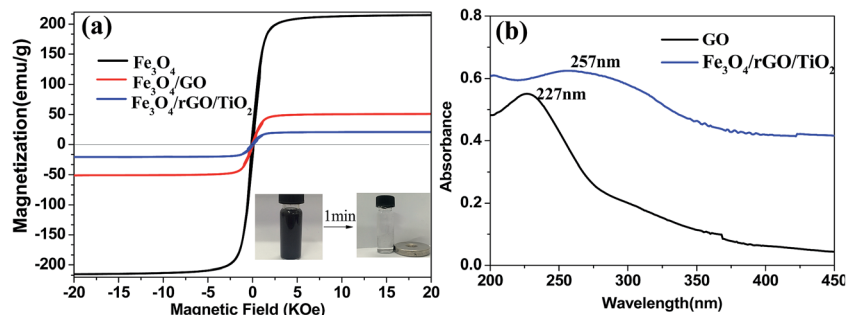
Fig. 3 (a) Magnetic hysteresis curves of Fe_3O_4 nanoparticles, Fe_3O_4/GO and $Fe_3O_4/rGO/TiO_2$ nanocomposite (inset: separation of particles dispersed in water by a magnet in 1 min). (b) UV-vis absorbance of GO and $Fe_3O_4/rGO/TiO_2$ nanocomposite.

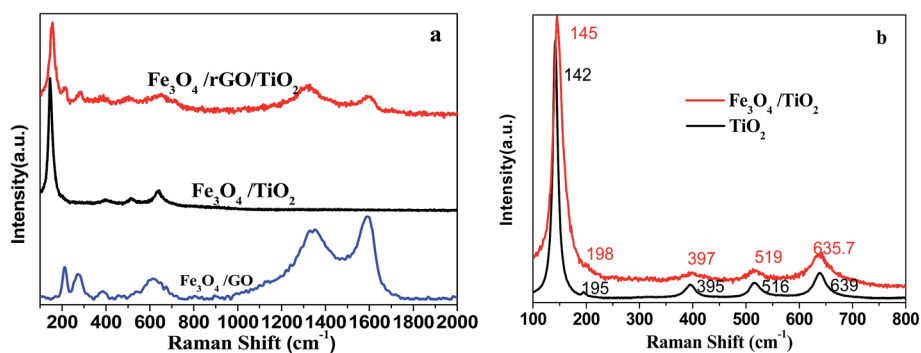**Fig. 4** Raman spectra of (a) Fe_3O_4/TiO_2, Fe_3O_4/GO, $Fe_3O_4/rGO/TiO_2$ nanocomposite (b) detail information of the Raman spectra of TiO_2 and Fe_3O_4/TiO_2 nanocomposite.

The specific surface areas of Fe_3O_4/GO and $Fe_3O_4/rGO/TiO_2$ hybrids were compared using Nitrogen adsorption–desorption measurements (Fig. 5). It is evident that $Fe_3O_4/rGO/TiO_2$ has similar isotherm to that of Fe_3O_4/GO, exhibiting type IV isotherms in IUPAC classification with a H1-type hysteresis loop, which conformed the mesostructures of the as-prepared materials.[3] Besides, the adsorption quantity of $Fe_3O_4/rGO/$ TiO_2 increased remarkably compared to that of the Fe_3O_4/GO, which demonstrate the synergistic effect of the TiO_2, GO and Fe_3O_4. Based on the isotherms, the BET surface areas of the

Fe_3O_4/GO and $Fe_3O_4/rGO/TiO_2$ were determined to be 6.08 and 33.47 m^2 g^{-1}, respectively. The average pore sizes of Fe_3O_4/GO and $Fe_3O_4/rGO/TiO_2$ composites are 18.29 and 11.48 nm, respectively.

In order to further confirm the chemical status and elemental composite of the as-prepared Fe_3O_4/TiO_2 and $Fe_3O_4/$ rGO/TiO_2 nanomaterials, the XPS measurement was carried out. As apparent from Fig. 6, in the full XPS spectra of the samples, the presence of Fe 2p1, Fe 2p3, O 1s, Ti 2p, and C 1s can be ascertained. In Fig. 6b, the Ti 2p core levels can be deconvoluted to a doublet (Ti $2p_{3/2}$ and Ti $2p_{1/2}$). However, the binding energy increased compared to the former literatures.[34,35] It may be caused by the interaction between Ti and the oxide functional groups of rGO, since the electronegativity of oxygen is higher than that of carbon. As for the C 1s peaks depicted in Fig. 6c, the C 1s peaks of Fe_3O_4/TiO_2 and $Fe_3O_4/rGO/TiO_2$ could be fitted by three peaks, which belong to the following functional groups: C=O (284.8 eV), C–O–C (286.9 eV) and O–C=O (288.7 eV). In Fig. 6d, the intensity peaks located at 710.8 eV and 724.8 eV belong to Fe $2p_{3/2}$ and Fe $2p_{1/2}$ respectively, implying the successful synthesis of Fe_3O_4 (ref. 36).
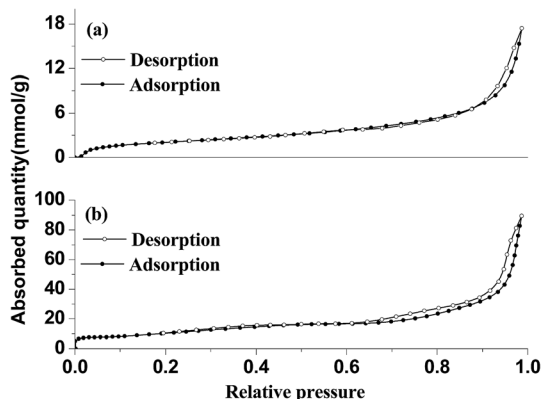
3.2 Photocatalytic performance

3.2.1 Photocatalytic activity of $Fe_3O_4/rGO/TiO_2$ nanocomposite. It has been widely accepted that the initial pH level of reaction system plays a key role in the degradation activity of
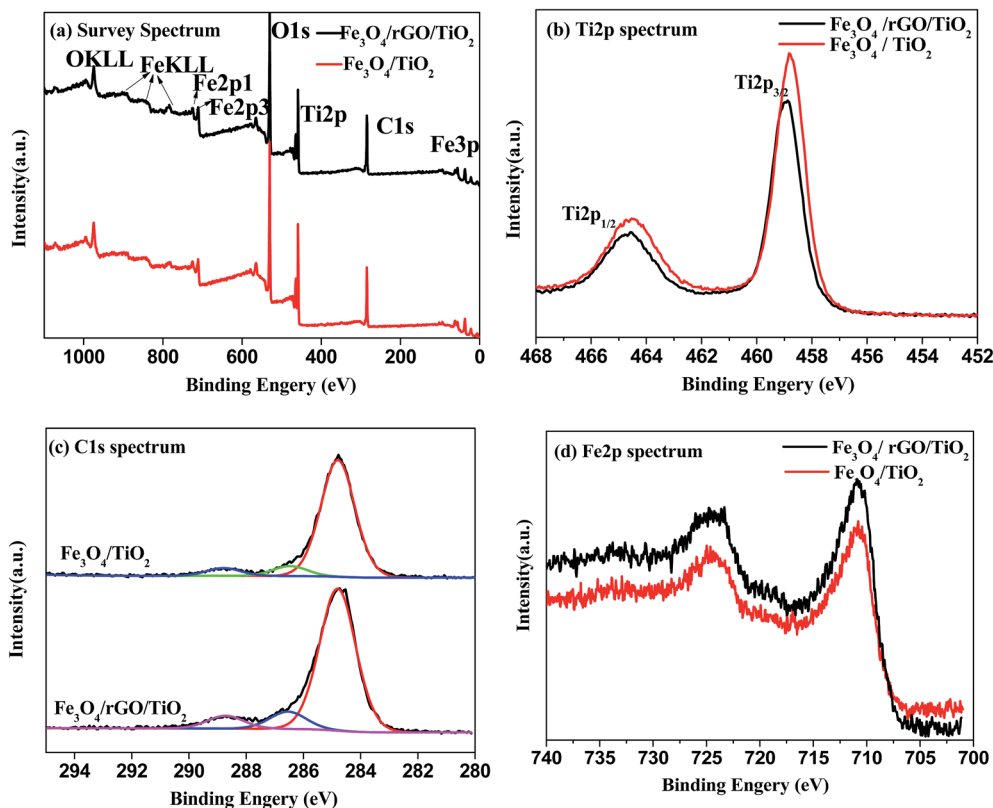

Fig. 5 N_2 adsorption–desorption isotherms of (a) Fe_3O_4/GO (b) $Fe_3O_4/rGO/TiO_2$ nanocomposite.

Fig. 6   XPS spectra of Fe_3O_4/TiO_2 and $Fe_3O_4/rGO/TiO_2$ nanocomposite: (a) full spectra of samples; (b) Ti 2p peaks; (c) C 1s peaks; (d) Fe 2p peaks.

catalyst toward TC-HCl.[37,38] In this study, the effect of initial pH value, ranging from 3 to 11, on the degradation rate of TC-HCl was investigated. The initial pH of pollutant solution was changed by adding 1 M H_2SO_4 or NaOH. As presented in Fig. 7a, the initial pH has a certain impact on TC-HCl removal. The degradation rate was achieved at 92.6% under pH 3. According to the pK_a values of the TC-HCl, the TC-HCl mainly exists as cation (TC^{3+}) when the pH < 3.3. Meanwhile, the zeta potential of $Fe_3O_4/rGO/TiO_2$ was negative. The electrostatic interactions between the catalyst and the TC-HCl was much stronger, thus enhancing the degradation rate. However, the degradation rate decreased slightly with the increasing initial pH values of the solutions from 5–11, under which condition the molecular structure of the TC-HCl presence as the form of $TCH^{2\pm}$, TCH^-, TC^{2-} rather than sole negative or positive particle. Besides, the release of ·OH from the reaction system also has a close connection with the pH values. It is well known that the acidic environment is much more favorable for the produce of ·OH from the reaction system, especially for the homogeneous Fenton system. Such a severe environment limits the application of the Fenton catalyst, and the as-prepared catalyst shows a high degradation rate under the neutral or alkaline environment, which can overcome the disadvantage of the homogeneous catalysis.

Fig. 7b illustrate the TC-HCl removal with various initial TC-HCl concentrations. It is obvious that the degradation rate of TC-HCl was related to the pollutant concentration, and the lower initial TC-HCl concentration in aqueous solution with the predetermined dosage of $Fe_3O_4/rGO/TiO_2$ and H_2O_2 favor the TC-HCl removal. The TC-HCl degradation rate decreased from 92.6% to 41.4% as the initial TC-HCl concentration increased from 20.0 to 120.0 mg L^{-1}. This can be attribute to the following reasons: the fixed amount of $Fe_3O_4/rGO/TiO_2$ and H_2O_2 produce the fixed ·OH amount, and the amount of TC-HCl molecules per unit volume increased with the increase of the TC-HCl concentration, leading to the decrease in the percentage of TC-HCl molecule involved into the reaction and the lower degradation rate.

The initial H_2O_2 also has a decisive effect on the degradation of the TC-HCl. As presented in Fig. 7c, TC-HCl removal reaches only 20% in the presence of $Fe_3O_4/rGO/TiO_2$ nanocomposite without any oxidant H_2O_2, which was attributed to the adsorption of TC-HCl molecules on $Fe_3O_4/rGO/TiO_2$ nanocomposite. The introduction of H_2O_2 into the TC-HCl solutions significantly accelerated the degradation of TC-HCl and the degradation performance was dependent on the initial H_2O_2 concentration in the pollutant solution. The degradation rate of TC-HCl increased when the H_2O_2 concentration increased from 20 mmol L^{-1} to 40 mmol L^{-1}, but decreased with further increasing H_2O_2 concentration to 60 mmol L^{-1} and 80 mmol L^{-1}. It is known that for the heterogeneous Fenton reaction the highly hydroxyl radicals, hence higher TC-HCl removal, are available at higher initial H_2O_2 concentrations. Nevertheless, H_2O_2 can also act as a hydroxyl radical scavenger as described in eqn (1) and (2), and can also take place the self-decomposition as described in eqn (3), so the further increase of the H_2O_2
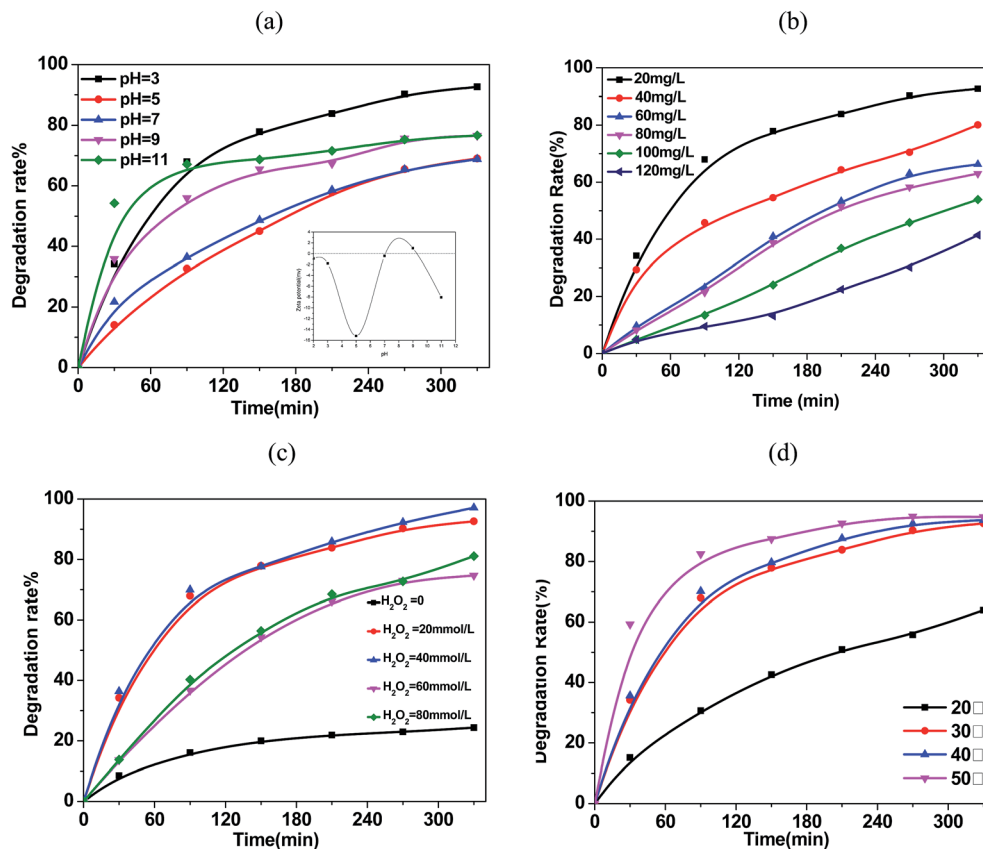
Fig. 7 Effects of (a) initial pH (inset: Zeta potential analysis of the Fe_3O_4/rGO/TiO_2 nanocomposite at different pH), (b) pollutant concentration, (c) H_2O_2 concentration and (d) temperature in degradation rates of TC-HCl. Experimental conditions: (a) catalyst loading = 400 mg L^{-1}; initial TC-HCl concentration = 20 mg L^{-1}; H_2O_2 concentration = 20 mmol L^{-1}; temperature = 30 ± 1 °C; (b) catalyst loading = 400 mg L^{-1}; H_2O_2 concentration = 20 mmol L^{-1}; temperature = 30 ± 1 °C; initial pH = 3; (c) catalyst loading = 400 mg L^{-1}; initial TC-HCl concentration = 20 mg L^{-1}; temperature = 30 ± 1 °C; pH = 3; (d) catalyst loading = 400 mg L^{-1}; initial TC concentration = 20 mg L^{-1}; H_2O_2 concentration = 20 mmol L^{-1}; pH = 3.

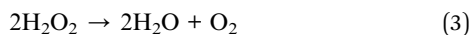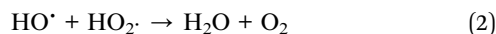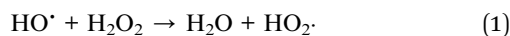concentration cannot result in the significant increase of hydroxyl radicals and the enhancement of the TC-HCl removal.[39]

$$HO^\bullet + H_2O_2 \rightarrow H_2O + HO_2\cdot \qquad (1)$$

$$HO^\bullet + HO_2\cdot \rightarrow H_2O + O_2 \qquad (2)$$

$$2H_2O_2 \rightarrow 2H_2O + O_2 \qquad (3)$$

Fig. 7d shown the effect of temperature on the degradation rate of TC-HCl by Fe_3O_4/rGO/TiO_2 nanocomposite. It is obvious that temperature has a strong effect on the degradation rate of Fe_3O_4/rGO/TiO_2 nanocomposite. The degradation rate increased with increasing temperature from 60% at 20 °C to 97% at 50 °C, which may be caused by the reason that the higher temperature enhanced the reaction rate between H_2O_2 and Fe_3O_4/rGO/TiO_2 nanocomposite, thus formationing more $\cdot$OH to take part in the reaction.

3.2.2 The possible pathway of TC-HCl degradation. The intermediates of TC-HCl were investigated by HPLC-MS and the results were illustrated in Fig. 8. The possible pathway is as follows (Fig. 9). First, the TC-HCl molecular deprotonated and the resulting molecular ion with $m/z = 445$ was found. Second, the electron–hole pairs were induced on the surface of Fe_3O_4/rGO/TiO_2 nanocomposite by the visible light irradiation, while the TC-HCl molecules in the solution ($m/z = 445$) were adsorbed onto the surface of Fe_3O_4/rGO/TiO_2,[40] and attacked by electrons or holes. In this process, various intermediates were formed as shown in Fig. 9.

3.2.3 Stability and reusability of Fe_3O_4/rGO/TiO_2 nanocomposites. The stability is one of the important factors to assess the quality of the catalysts since the photocorrosion or photodissolution might occur on the photocatalyst surface in the photocatalytic process.[41] So we conducted a series of experiment to investigate the stability and reusability of the Fe_3O_4/rGO/TiO_2 nanocomposites. In the typical procedure of the stability experiment, the Fe_3O_4/rGO/TiO_2 nanocomposites was separated by centrifugation after each cycle, dried at 60 °C overnight and be used without further treatment. As apparent from Fig. 10a, the photocatalytic efficiency of Fe_3O_4/rGO/TiO_2 nanocomposites decreased slightly in the five cycles, which could be ascribed to the following two reasons: (1) the
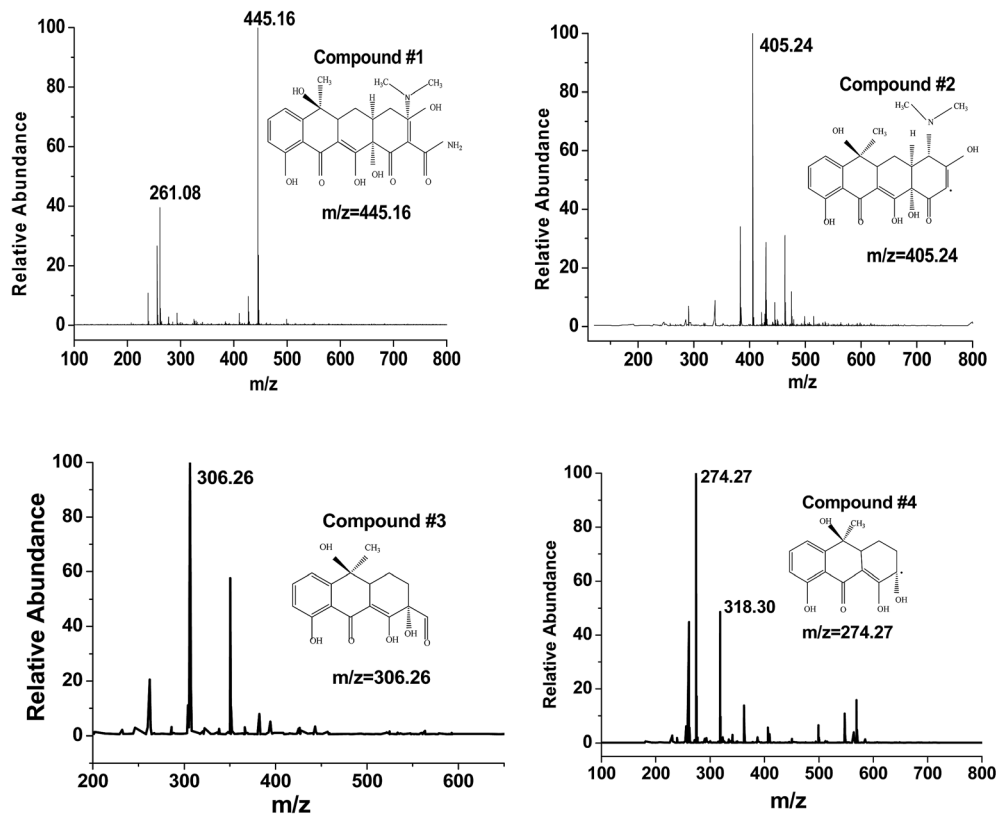
Fig. 8   Principal by-products of TC-HCl degradation detected by LC-MS.

photocorrosion of the Fe_3O_4/rGO/TiO_2 nanocomposites in the reaction system; (2) the TC-HCl strongly adsorbed on the surface of the catalysts and occupy the active sites, thus reducing the photocatalytic activity. In addition, the Fe leaching in the reaction system in the first cycle is almost negligible (Fig. 10b), which can get rid of the secondary wastes that caused in the traditional Fenton process. Furthermore, the XRD and FT-IR are also utilized to test its stability. The results are presented in Fig. 11, there are almost no significant changes in the XRD pattern and FT-IR spectrum of the Fe_3O_4/rGO/TiO_2

catalyst before and after degradation, suggesting that the as-prepared Fe_3O_4/rGO/TiO_2 hybrid reveals excellent stability and great potential application value.

3.3   Possible photo-degradation mechanism of TC-HCl

3.3.1   Quenching test. It is widely acknowledged that the active species of ˙OH, h^+, ˙O_2^-, e^- play the main role in the photocatalytic oxidation.[41,42] In order to make sure the main active species responsible for TC-HCl degradation, a series of
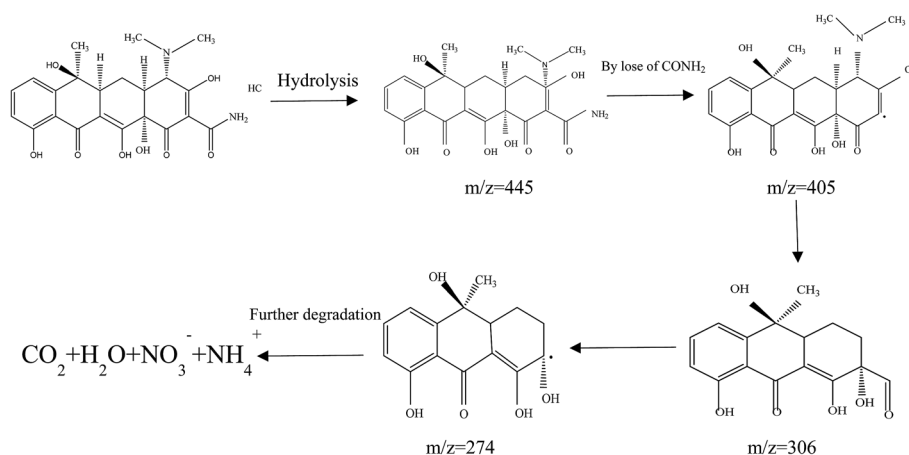

Fig. 9   Proposed TC-HCl degradation pathways in the Fe_3O_4/rGO/TiO_2/H_2O_2 system.

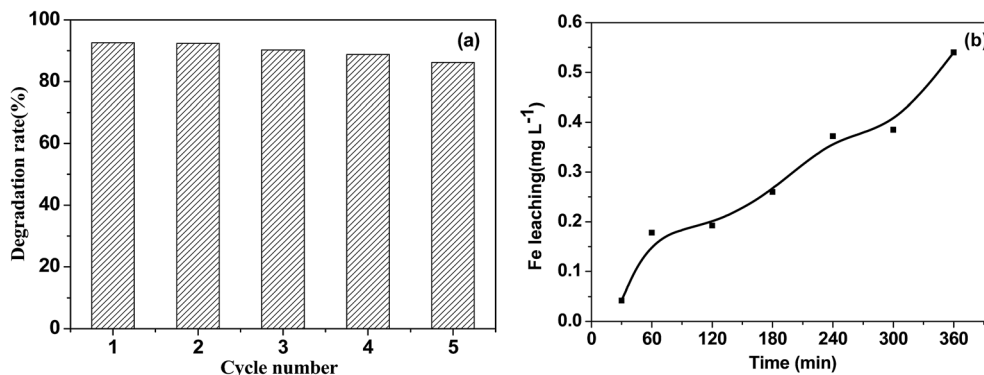**Fig. 10** (a) The stability of the Fe$_3$O$_4$/rGO/TiO$_2$ photocatalyst for the discoloration of TC-HCl (b) the Fe leaching from Fe$_3$O$_4$/rGO/TiO$_2$ photocatalyst in the first cycle as a function of time.

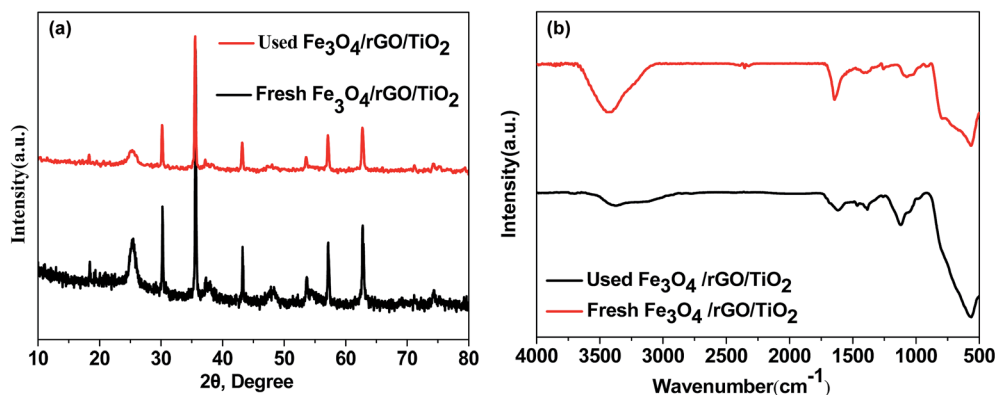**Fig. 11** (a) XRD pattern and (b) FT-IR spectra of the pristine and used Fe$_3$O$_4$/rGO/TiO$_2$ photocatalyst.

trapping experiments were carried out by adding some corresponding scavengers to the degradation system. Fig. 12 illustrates the results of trapping experiments over the Fe$_3$O$_4$/rGO/TiO$_2$ photocatalyst reaction system. When 100 mM triethanolamine (TEOA) scavenger for h$^+$ is introduced into the reaction system, the degradation rate decreased slightly by 16% (entry b in Fig. 12) compared to the pristine reaction system without

radical scavengers (entry a in Fig. 12). Similarly, the degradation rate of TC-HCl is also declined by 28% (entry c in Fig. 12) when the iso-propanol (IPA), scavenger for $^\bullet$OH, is added into the system. However, the photocatalytic activity of Fe$_3$O$_4$/rGO/TiO$_2$ is significantly inhibited when BQ (a quencher of $^\bullet$O$_2^-$) or DMSO (a quencher of e$^-$) is introduced into the photocatalytic reaction system. From the above results, it can be concluded
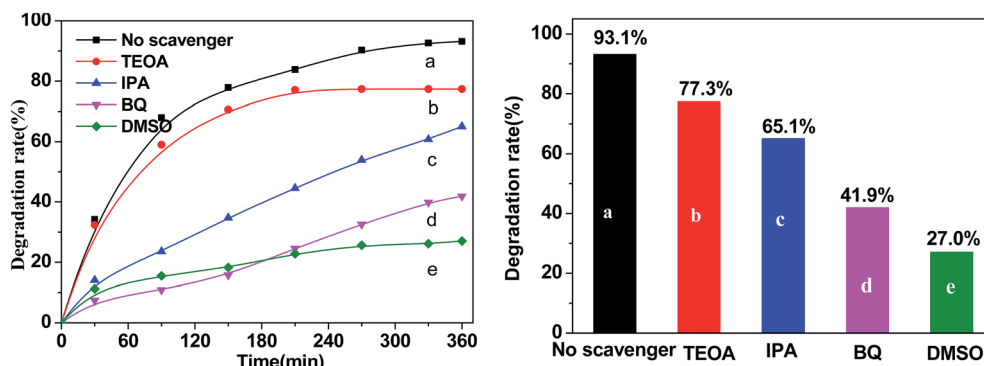

Fig. 12 Photocatalytic degradation ratios of TC-HCl by Fe$_3$O$_4$/rGO/TiO$_2$ using different radical scavengers (a) reaction in the absence of radical scavengers, (b) reaction with 100 mM TEOA as a scavenger for h$^+$, (c) reaction with 100 mM IPA for $^\bullet$OH, and (d) reaction with 0.2 mM BQ for $^\bullet$O$_2^-$ (e) reaction with 100 mM DMSO as a scavenger for e$^-$ under visible light irradiation for 360 min.
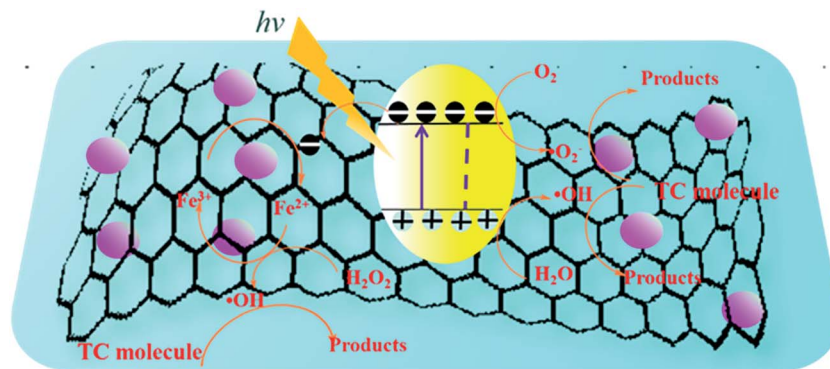
Fig. 13 Proposed schematic illustration showing the reaction mechanism for photocatalytic degradation of TC-HCl over the Fe_3O_4/rGO/TiO_2 nanocomposites in which pink spheres, yellow oval and black sheet represent Fe_3O_4 nanoparticles, TiO_2 nanoparticles and rGO, respectively.

that the e$^-$ radicals and $^\cdot O_2{}^-$ radicals should be the two main actives species during photocatalytic degradation of TC-HCl by the Fe_3O_4/rGO/TiO_2 nanocomposites under visible light irradiation.

3.4 Proposed mechanism of photocatalysis with the photocatalyst

On the basis of the discussion of quenching test, the possible photocatalytic mechanism schemes of Fe_3O_4/rGO/TiO_2 is proposed, as depicted in Fig. 13. When the Fe_3O_4/rGO/TiO_2 were subjected to visible light irradiation, the excitation of an electron from the valence band to the conduction band resulting the generation of electron (e$^-$) in the conduction band (CB) and holes (h$^+$) in the valence band (VB).[43] For Fe_3O_4/rGO/TiO_2 system, the electron (e$^-$) transferred to rGO sheet due to the excellent electrical conductivity of rGO, and then take part in the reduction reaction, thus inhibiting the recombination of the electron–hole pairs and making the electron transfer process more efficient.[44] Besides, the rGO could also transfer the photogenerated electron to the surface of Fe_3O_4 and reduce the Fe^{3+} to Fe^{2+} because of the superior intimate contact between Fe_3O_4 and rGO.[45] Furthermore, the generate Fe^{2+} may be able to reduce the H_2O_2 to $^\cdot OH$, which finally degrade organic pollutants. Of cause, it is clear from the Fig. 13 that e$^-$ in CB can react with O_2 in the aqueous solution to produce $^\cdot O_2{}^-$ to degrade the pollutant, which is in agreement with the result of trapping experiment. Meanwhile, the holes generated on the surface of TiO_2 nanoparticle oxidize pollutant molecules.

4 Conclusion

In conclusion, Fe_3O_4/rGO/TiO_2 photocatalyst was successfully synthesized by a simple two-step process, an electrostatic self-assemble and hydrothermal method. The uniform Fe_3O_4 nanoparticles was firstly deposited on the surface of GO sheet through a facile electrostatic self-assembly method. Then the TiO_2 particles was anchored on the surface of the Fe_3O_4/rGO through hydrothermal reaction. The photocatalytic activity of the as-prepared ternary catalyst Fe_3O_4/rGO/TiO_2 has been explored for the degradation of TC-HCl. The Fe_3O_4/rGO/TiO_2

photocatalyst shows superior activity in the neutral or alkaline environment. The enhanced catalytic activity of our catalyst is due to the synergistic effect of photo-Fenton reaction and electron transportation and conducting ability as a result of deposition of graphene. The products of TC-HCl degradation were identified by LC-MS and the possible pathway and mechanism of photocatalysis of the TC-HCl was proposed. The result reveals that the e$^-$ radicals and $^\cdot O_2{}^-$ radicals should be the two main actives species during photocatalytic degradation of TC-HCl by the Fe_3O_4/rGO/TiO_2 nanocomposites under visible light irradiation. In addition, the catalyst is reusable and shows efficiency up to 5 cycles. We believe the strategy in our work can provide insight into designing the novel photocatalysts for large-scale degradation of organic pollutants under visible light.

Acknowledgements

References

1 Y. Chen and K. Liu, *Chem. Eng. J.*, 2016, **302**, 682–696.
2 B. Luo, D. Xu, D. Li, G. Wu, M. Wu, W. Shi and M. Chen, *ACS Appl. Mater. Interfaces*, 2015, **7**, 17061–17069.
3 Q. Liu, L. Bin Zhong, Q. B. Zhao, C. Frear and Y. M. Zheng, *ACS Appl. Mater. Interfaces*, 2015, **7**, 14573–14583.
4 H. Li, D. Zhang, X. Han and B. Xing, *Chemosphere*, 2014, **95**, 150–155.
5 S. K. Bajpai and M. Bhowmik, *J. Macromol. Sci., Part A: Pure Appl. Chem.*, 2011, **48**, 108–118.
6 R. Levine, Civil Engineering Theses, Dissertations, and Student Research, 2016.
7 F. Chen, Q. Yang, X. Li, G. Zeng, D. Wang, C. Niu, J. Zhao, H. An, T. Xie and Y. Deng, *Appl. Catal., B*, 2017, **200**, 330–342.
8 M. Haidar, A. Dirany, I. Sirés, N. Oturan and M. A. Oturan, *Chemosphere*, 2013, **91**, 1304–1309.

This journal is © The Royal Society of Chemistry 2017

9 S. zhong Li, X. yan Li and D. zuo Wang, *Sep. Purif. Technol.*, 2004, **34**, 109–114.

10 H. Hou, F. Gao, L. Wang, M. Shang, Z. Yang, J. Zheng and weiyou yang, *J. Mater. Chem. A*, 2016, **4**, 6276–6281.

11 M. Xing, X. Li and J. Zhang, *Sci. Rep.*, 2014, **4**, 5493.

12 W. T. Sun, A. Yu, H. Y. Pan, X. F. Gao, Q. Chen and L. M. Peng, *J. Am. Chem. Soc.*, 2008, **130**, 1124–1125.

13 S. Rawalekar and T. Mokari, *Adv. Energy Mater.*, 2013, **3**, 12–27.

14 M. Ni, M. K. H. Leung, D. Y. C. Leung and K. Sumathy, *Renewable Sustainable Energy Rev.*, 2007, **11**, 401–425.

15 X. Zong, H. Yan, G. Wu, G. Ma, F. Wen, L. Wang and C. Li, *J. Am. Chem. Soc.*, 2008, **130**, 7176–7177.

16 A. Fujishima, X. Zhang and D. A. Tryk, *Surf. Sci. Rep.*, 2008, **63**, 515–582.

17 R. Daghrir, P. Drogui and D. Robert, *Ind. Eng. Chem. Res.*, 2013, **52**, 3581–3599.

18 J. Deng, X. Wen and Q. Wang, *Mater. Res. Bull.*, 2012, **47**, 3369–3376.

19 N. Zhang, Y. Zhang and Y.-J. Xu, *Nanoscale*, 2012, **4**, 5792.

20 H. Deng, X. Li, Q. Peng, X. Wang, J. Chen and Y. Li, *Angew. Chem., Int. Ed.*, 2005, **44**, 2782–2785.

21 Y. Zhang, Z. Tang, X Fu and Y. Xu, *ACS nano*, 2010, **4**, 7303–7314.

22 M. Zhao, L. Figueroa-Cosme, A. O. Elnabawy, M. Vara, X. Yang, L. T. Roling, M. Chi, M. Mavrikakis and Y. Xia, *Nano Lett.*, 2016, **16**, 5310–5317.

23 R. K. Das, J. P. Kar and S. Mohapatra, *Ind. Eng. Chem. Res.*, 2016, **55**, 5902–5910.

24 G. Fu, L. Ding, Y. Chen, J. Lin, Y. Tang and T. Lu, *CrystEngComm*, 2014, **16**, 1606–1610.

25 A. A. Al-Kahtani and M. F. Abou Taleb, *J. Hazard. Mater.*, 2016, **309**, 10–19.

26 T. Xin, M. Ma, H. Zhang, J. Gu, S. Wang, M. Liu and Q. Zhang, *Appl. Surf. Sci.*, 2014, **288**, 51–59.

27 W. Li, J. Yang, Z. Wu, J. Wang, B. Li, S. Feng, Y. Deng, F. Zhang and D. Zhao, *J. Am. Chem. Soc.*, 2012, **134**, 11864–11867.

28 L. Tan, X. Zhang, Q. Liu, X. Jing, J. Liu, D. Song, S. Hu, L. Liu and J. Wang, *Colloids Surf., A*, 2015, **469**, 279–286.

29 G. Mishra, K. M. Parida and S. K. Singh, *ACS Sustainable Chem. Eng.*, 2015, **3**, 245–253.

30 A. Tayyebi, M. Outokesh, S. Moradi and A. Doram, *Appl. Surf. Sci.*, 2015, **353**, 350–362.

31 M. Wang, J. Han, H. Xiong and R. Guo, *Langmuir*, 2015, **31**, 6220–6228.

32 R. Ren, Z. Wen, S. Cui, Y. Hou, X. Guo and J. Chen, *Sci. Rep.*, 2015, **5**, 10714.

33 D. R. Tobergte and S. Curtis, *J. Chem. Inf. Model.*, 2013, **53**, 1689–1699.

34 G. T. S. How, A. Pandikumar, H. N. Ming and L. H. Ngee, *Sci. Rep.*, 2014, **4**, 5044.

35 Z. Xu, C. Huang, L. Wang, X. Pan, L. Qin, X. Guo and G. Zhang, *Ind. Eng. Chem. Res.*, 2015, **54**, 4593–4602.

36 W. Zhang, X. Li, R. Zou, H. Wu, H. Shi, S. Yu and Y. Liu, *Sci. Rep.*, 2015, **5**, 11129.

37 P. H. Chang, Z. Li, J. S. Jean, W. T. Jiang, C. J. Wang and K. H. Lin, *Appl. Clay Sci.*, 2012, **67–68**, 158–163.

38 Y. Ma, N. Gao and C. Li, *Environ. Eng. Sci.*, 2012, **29**, 357–362.

39 L. Hu, D. Xu, L. Zou, H. Yuan and X. Hu, *Acta Phys.-Chim. Sin.*, 2015, **31**, 771–782.

40 K. Dai, T. Peng, H. Chen, J. Liu and L. Zan, *Environ. Sci. Technol.*, 2009, **43**, 1540–1545.

41 M. Zhou, D. Han, X. Liu, C. Ma, H. Wang, Y. Tang, P. Huo, W. Shi, Y. Yan and J. Yang, *Appl. Catal., B*, 2015, **172–173**, 174–184.

42 G. Zhang, W. Guan, H. Shen, X. Zhang, W. Fan, C. Lu, H. Bai, L. Xiao, W. Gu and W. Shi, *Ind. Eng. Chem. Res.*, 2014, **53**, 5443–5450.

43 A. L. Linsebigler, A. L. Linsebigler, J. T. Yates Jr, G. Lu, G. Lu and J. T. Yates, *Chem. Rev.*, 1995, **95**, 735–758.

44 S. Zhong, W. Jiang, M. Han, G. Liu, N. Zhang and Y. Lu, *Appl. Surf. Sci.*, 2015, **347**, 242–249.

45 Y. Park, S.-H. Kang and W. Choi, *Phys. Chem. Chem. Phys.*, 2011, **13**, 9425–9431.